

# Structural and functional characterization of (110)-oriented epitaxial $\text{La}_{2/3}\text{Ca}_{1/3}\text{MnO}_3$ electrodes and $\text{SrTiO}_3$ tunnel barriers

I. C. Infante,<sup>a)</sup> F. Sánchez, and J. Fontcuberta

*Institut de Ciència de Materials de Barcelona, CSIC, Campus UAB, Bellaterra 08193, Spain*

S. Fusil, K. Bouzehouane, G. Herranz, and A. Barthélémy

*Unité Mixte de Physique CNRS/Thales, Route Départementale 128, 91767 Orsay, France*

S. Estradé, J. Arbiol, and F. Peiró

*Departament d'Electrònica, Universitat de Barcelona, Diagonal 647, Barcelona 08028, Spain*

R. J. O. Mossaneck and M. Abbate

*Departamento de Física, Universidade Federal do Paraná, Caixa Postal 19091, 81531-990 Curitiba PR, Brazil*

M. Wojcik

*Institute of Physics, Polish Academy of Sciences, Al. Lotników 32/46, 02 668 Warszawa, Poland*

(Received 22 January 2007; accepted 8 March 2007; published online 3 May 2007)

$\text{La}_{2/3}\text{Ca}_{1/3}\text{MnO}_3$  (LCMO) films have been deposited on (110)-oriented  $\text{SrTiO}_3$  (STO) substrates. X-ray diffraction and high-resolution electron microscopy reveal that the (110) LCMO films are epitaxial and anisotropically in-plane strained, with higher relaxation along the  $[1-10]$  direction than along the  $[001]$  direction; x-ray absorption spectroscopy data signaled the existence of a single intermediate  $\text{Mn}^{3+/4+}$  3d-state at the film surface. Their magnetic properties are compared to those of (001) LCMO films grown simultaneously on (001) STO substrates. It is found that (110) LCMO films present a higher Curie temperature ( $T_C$ ) and a weaker decay of magnetization when approaching  $T_C$  than their (001) LCMO counterparts. These improved films have been subsequently covered by nanometric STO layers. Conducting atomic-force experiments have shown that STO layers, as thin as 0.8 nm, grown on top of the (110) LCMO electrode, display good insulating properties. We will show that the electric conductance across (110) STO layers, exponentially depending on the barrier thickness, is tunnel-like. The barrier height in STO (110) is found to be similar to that of STO (001). These results show that the (110) LCMO electrodes can be better electrodes than (001) LCMO for magnetic tunnel junctions, and that (110) STO are suitable insulating barriers. © 2007 American Institute of Physics. [DOI: [10.1063/1.2723192](https://doi.org/10.1063/1.2723192)]

## I. INTRODUCTION

The discovery of the colossal magnetoresistance in manganites ( $\text{La}_{1-x}\text{A}_x\text{MnO}_3$ ) opened a wider horizon of possibilities for the integration of this family of materials into spintronic devices. Its half-metallic ferromagnetic character offered the possibility to design almost ideal magnetic tunnel junctions (MTJs), as its fully spin-polarized conduction band could lead to the largest magnetoresistance in MTJ. Certainly, MTJs were soon made using the most common  $\text{SrTiO}_3$  (STO) material, not only as the substrate—with a typical (001) crystal orientation in epitaxial growth of manganite films—but also as the insulating layer in the heterostructures. Disappointingly, in spite of the large output value of the tunnel magnetoresistance obtained at low temperature, it has been repeatedly found that it decreases rapidly with temperature, vanishing at temperatures well below the Curie temperature ( $T_C$ ) of the manganite electrodes.<sup>1-4</sup>

The ultimate reasons for this behavior have not been definitely settled. The intrinsic strong tendency of electronic phase separation present in manganites<sup>5</sup> could be at the origin of this decrease in the tunnel properties at higher tem-

peratures. Interface effects, such as substrate-induced strain,<sup>3,6-9</sup> can further promote electronic or chemical phase segregations. Electronic phase separation could also be driven by electronic interaction with substrates. Indeed, it has been recently pointed out that charge density gradients or polarity discontinuities<sup>10</sup> across interfaces in oxide-based heterostructures may be a driving force for charge redistribution. In any event, it is worth noting that most MTJs based on manganites have used STO (001) as substrate. After suitable substrate treatment, a single terminated  $\text{TiO}_2$  surface can be obtained.<sup>11</sup> Electron counting shows that  $\text{TiO}_2$  is a neutral surface. In contrast, the upper growing  $(\text{La}_{1-x}\text{A}_x)\text{O}$  and  $(\text{MnO}_2)$  are charged:  $+(1-x)$  and  $-(1-x)$ , respectively. Therefore, it is clear that, due to the built-in potential, charge redistribution within the manganite layer may occur, modifying its properties. We further notice that its strength will be dependent on the precise doping ( $x$ ) level.

On the other hand,  $\text{La}_{1-x}\text{A}_x\text{MnO}_3$  manganites grown on (001) surfaces display a biaxial in-plane magnetic anisotropy.<sup>12,13</sup> This situation is far from optimal for practical application of MTJs, where uniaxial anisotropy would be preferred. Therefore, it follows that although  $\text{La}_{1-x}\text{A}_x\text{MnO}_3$ (001) layers on STO (001) substrates have

<sup>a)</sup>Electronic mail: [icanerin@icmab.es](mailto:icanerin@icmab.es)

been the workhorse of research in manganite-based MTJ, this choice does not appear to be unquestionable. Instead, STO (110) substrates could, in principle, constitute a better alternative.

We note that free (110) surfaces in STO, SrTiO<sub>3</sub>, and O<sub>2</sub> are not neutral but charged: +4 and −4, respectively. Epitaxial stacking of a La<sub>1−x</sub>A<sub>x</sub>MnO<sub>3</sub> oxide on the (110) STO substrate would not lead to any polarity discontinuity as the growing layers (La<sub>1−x</sub>A<sub>x</sub>MnO and O<sub>2</sub>) are also polar (+4 and −4) for any doping level. On the other hand, (110) surfaces of STO and of La<sub>1−x</sub>A<sub>x</sub>MnO<sub>3</sub> display not square symmetry but rectangular, so one could expect to obtain magnetic layers with reduced magnetic symmetry. Finally, the atomic sequence along the two orthogonal directions ([001] and [1−10]) in (110) surfaces radically differs: Mn–O–Mn separated by a distance  $a_p$  along the [001] direction ( $a_p$  being the pseudocubic unit cell length), and Mn–Mn separated by  $a_p\sqrt{2}$  along the [1−10] direction. As a consequence, one could expect that the elastic properties of the manganite layer could differ along these two directions, eventually leading to the possibility of tailoring the in-plane anisotropy.

Manganite films and heterostructures with orientations other than (001) have been scarcely investigated. Nevertheless, it has been shown that (110)-oriented La<sub>2/3</sub>Ca<sub>1/3</sub>MnO<sub>3</sub> (LCMO) films present a uniaxial in-plane anisotropy;<sup>14–17</sup> it has also been shown that the anisotropic magnetoresistance<sup>14,18</sup> is itself anisotropic. Interestingly enough, Mn<sup>55</sup> nuclear magnetic resonance (NMR) experiments on (110)-oriented LCMO films on STO (110) have failed to detect the presence of manganese in Mn<sup>4+</sup> ionization state on NMR time scale (10<sup>−9</sup> s), which would have been a sign of charge localization in the material, thus suggesting that the (110) films are electronically homogeneous.<sup>17</sup> Similar experiments on LCMO (001) films unequivocally revealed evidence of electronic phase separation, with distinguishable Mn<sup>4+</sup> and Mn<sup>3+</sup> states.<sup>6,7</sup> A recent study<sup>19</sup> reports that even at defective areas (dislocations) in LCMO (110) films the stoichiometry is kept similar to the rest of the film.

Aiming to contribute to the development of MTJ using (110) manganites, we report here the progress in the fabrication of LCMO electrodes and STO barriers on STO (110) substrates. We will show that the magnetic properties (magnetization and  $T_C$ ) of the (110) LCMO electrodes are better than LCMO (001) electrodes grown simultaneously. Afterwards, we will address the magnetic anisotropy of these films confirming the expected uniaxial character. We will subsequently report on growth of nanometric STO barriers and explore their transport properties using a conducting atomic force microscopy (CAFM) setup. The energy barrier for transport across STO (110) barrier will be derived. In short, the feasibility of STO (110) layer as a tunnel barrier in (110)-oriented LCMO-based MTJs will be demonstrated.

## II. EXPERIMENTAL

Thin LCMO electrodes and STO/LCMO bilayers were deposited by rf magnetron sputtering. Films were grown on STO (110) substrates, which were previously annealed in air at 1000 °C for 2 h. Deposition conditions for LCMO and

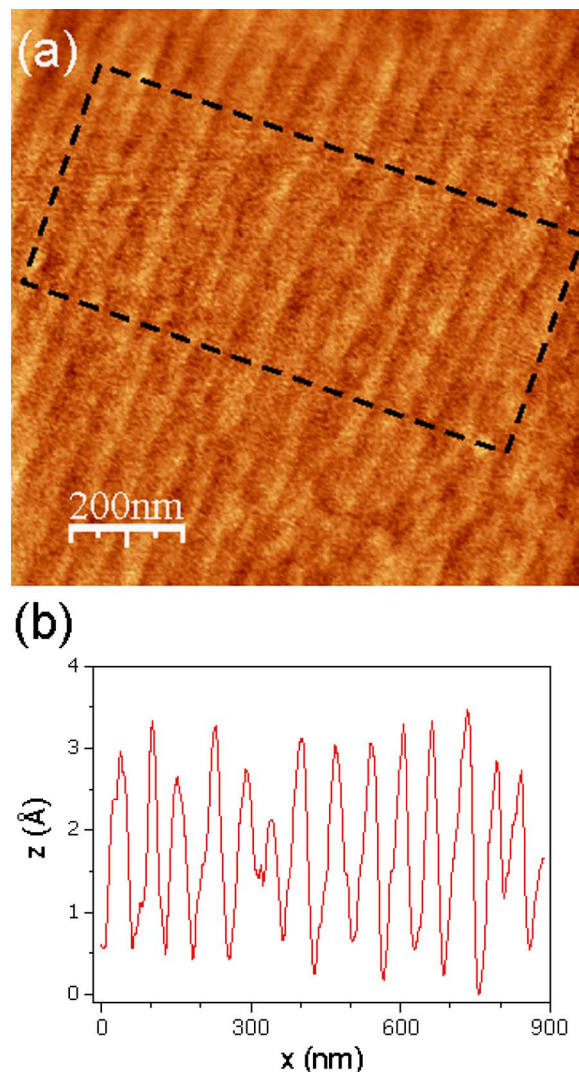


FIG. 1. (a) AFM topographic image ( $1 \times 1$ )  $\mu\text{m}^2$  of the STO (110) surface after annealing at 1000 °C during 2 h in air. (b) Average profile calculated from a series of height profiles parallel to the long side of the rectangle displayed in (a).

STO layers were set to 800 °C as substrate temperature and 330 mTorr as chamber pressure (80% Ar, 20% O<sub>2</sub>). Bilayers were prepared in a single process; the STO was deposited consecutively on top of the LCMO electrode. After deposition, the samples were *in situ* annealed at 800 °C during 1 h under an oxygen pressure of 350 Torr. Growth rate for LCMO and STO was 1.8 and 2.1 Å/min, respectively, determined from small-angle x-ray reflectometry (XRR) on single films of proper thickness. Afterwards, the thickness of the LCMO electrodes and the nanometric STO barriers was controlled by the deposition time.

Morphological and structural characterization of the substrates and films has included atomic force microscopy (AFM), x-ray diffraction (XRD), and high-resolution transmission electron microscopy (HRTEM). LCMO films were measured by x-ray absorption spectroscopy (XAS) at the SGM beam line in the LNLS (Brazil). The base pressure in the experimental chamber was in the low 10<sup>−9</sup> mbar range. The mean-probing depth of the total-electron-yield method is about 20–50 Å.<sup>20</sup> The energy resolution of the spherical

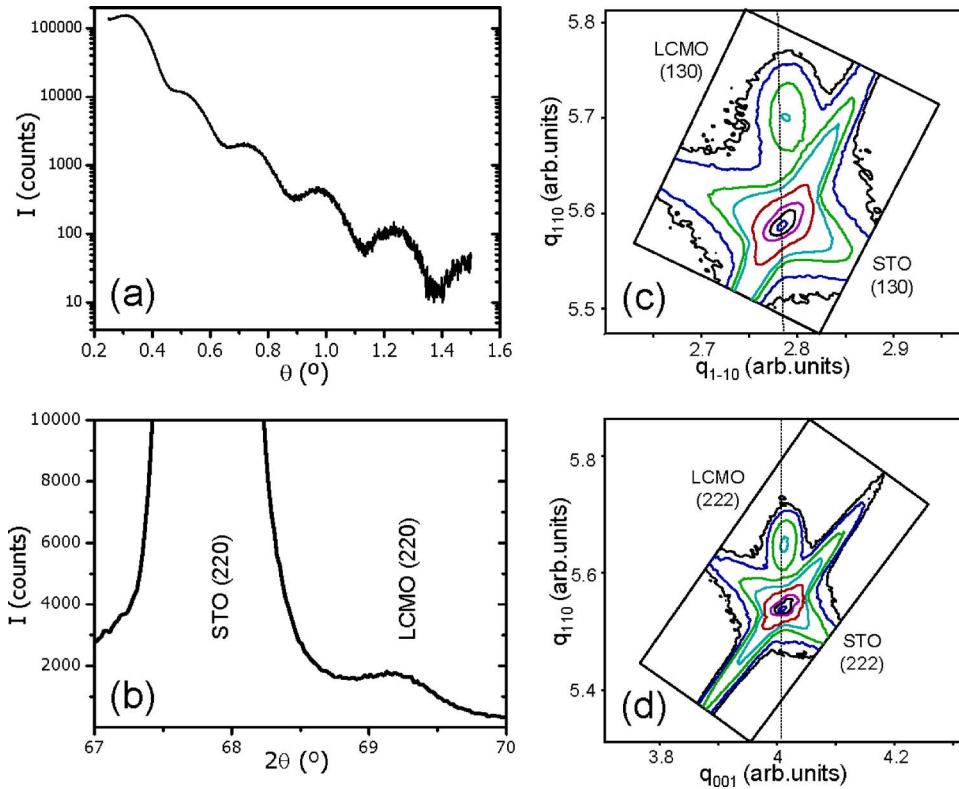


FIG. 2. X-ray reflectometry and x-ray diffraction results from the same 17 nm thick LCMO film: (a) Reflectometry curve; (b) detail of the XRD  $\theta$ - $2\theta$  scan showing (220) peak; (c) and (d) are reciprocal space maps (RSM) around (130) and (222) LCMO reflections, respectively.

grating monochromator was approximately 0.5–0.6 eV. The energy scale was calibrated using the peak positions in the parent  $\text{LaMnO}_3$  compound. The spectra were normalized to the maximum after a constant background subtraction. The XAS spectra of LCMO (110) films have been compared with those of LCMO (001) films that were simultaneously prepared on STO (001) substrates. Magnetic properties of the LCMO electrodes were studied with a SQUID magnetometer (Quantum Design). Conducting atomic force microscopy (CAFM) was used to record electrical resistance maps of nanometric STO barriers on LCMO (110). Resistance maps were obtained using  $\text{Si}_3\text{N}_4$ -coated tips coated by boron-doped polycrystalline diamond, with typical spring constant of 40 N/m and applying a force of around 2  $\mu\text{N}$ .

### III. RESULTS AND DISCUSSION

A topographic AFM image of the substrate, after the annealing in air at 1000 °C for 2 h, is shown in Fig. 1(a). Steps between terraces are very straight, with the meandering being low. The height profile in Fig. 1(b) corresponds to an average of the height profiles along lines parallel to the long edge of the rectangle displayed in the topographic image. Average step height is around 2.5 Å, close to the interplane distance of (110) planes ( $d_{110} = a_{\text{STO}}/\sqrt{2} = 2.76$  Å). Note that in the case of the steps slightly meandering the average height is lower than the real step height. Since terraces are around 60 nm wide, the miscut angle is estimated to be  $\sim 0.25^\circ$ . Thus, the simple thermal treatment we have done of the (110) STO substrate has led to atomically flat surfaces with regularly ordered steps. We emphasize that the substrates were treated under oxygen-rich atmosphere. Mukunoki *et al.*<sup>21</sup> recently reported that a strongly reducing atmo-

sphere was required to obtain flat STO (110) surfaces when using substrates with a smaller miscut angle ( $\sim 0.1^\circ$ ) and wider ( $\sim 200$  nm) terraces.

The XRR data measured from a LCMO(110) film are plotted in Fig. 2(a). Clear oscillations are observed; the film thickness  $t$  can be calculated from minima position. For the particular case of Fig. 2(a), the thickness of the LCMO film is found to be 17 nm. The films are epitaxial and [110] out-of-plane oriented. Figure 2(b) shows an XRD  $\theta$ - $2\theta$  scan around the LCMO (220) reflection corresponding to the  $t = 17$  nm film. In larger angular scans, only the ( $h$  $h$ 0) reflections from the substrate and the film were detected. No traces of other phases or orientations were observed. LCMO films of different thickness (8–150 nm) have also been prepared and exhaustively characterized. Data, which have been reported elsewhere,<sup>15–17</sup> indicate that fully textured (110) epitaxial films can be obtained even with thickness as large as 150 nm. Here, we will focus the discussion on LCMO electrodes with thicknesses in the 11–21 nm range. The out-of-plane interplanar distance, extracted from Fig. 2(b), is  $d_{110} = 2.705$  Å. Assuming a pseudocubic unit cell for bulk LCMO ( $a_{\text{LCMO}} \approx 3.863$  Å),<sup>22</sup> the corresponding interplanar distance is  $d_{110} = 2.731$  Å; therefore, the out-of-plane interplanar distance is shortened with respect to the bulk, indicating a compressive strain of  $\varepsilon[110] = -0.9\%$ .

The shrinkage of the cell along the out-of-plane direction [110] results from the in-plane tensile strain caused by the larger cell parameter of the substrate. Indeed,  $a_{\text{STO}} = 3.905$  Å and  $a_{\text{LCMO}}(\text{bulk}) = 3.863$  Å, thus giving rise to a bulk lattice mismatch [defined as  $(a_{\text{subs}} - a_{\text{bulk}})/a_{\text{bulk}}$ ] of about +1.2%. To determine the actual in-plane and out-of-plane cell parameters of the LCMO film, we have collected XRD reciprocal space maps (RSM). Figure 2(c) shows the RSM



around the LCMO (130) (top peak) and the STO (130) reflections (bottom peak). The substrate peak being a reference, the vertical and the horizontal coordinates of the LCMO (130) peak in the RSM allows one to evaluate the out-of-plane  $d_{\text{LCMO}}[110]$  and the in-plane  $d_{\text{LCMO}}[1-10]$  parameters. The  $d_{\text{LCMO}}[110]$  distance ( $=2.705 \text{ \AA}$ ) extracted from the RSM is coincident with that calculated from symmetric reflections. The in-plane  $d_{\text{LCMO}}[1-10]$  parameter is found to be  $2.752 \text{ \AA}$ , close to the corresponding distance in the substrate ( $d_{\text{STO}}[1-10]=2.761 \text{ \AA}$ ). The strain  $\varepsilon[1-10]=+0.8\%$  is slightly lower in magnitude than that expected from the bulk lattice mismatch, which signals a partial lattice relaxation along the  $[1-10]$  direction. To determine the cell parameters along the orthogonal in-plane direction  $[001]$ , a suitable RSM has been collected around the (222) peak [shown in Fig. 2(d)]. It turns out that  $d_{\text{LCMO}}[001] \approx 3.901 \text{ \AA}$ , very close to  $d_{\text{STO}}[001] \approx 3.905 \text{ \AA}$ , thus signaling an almost fully strained film along the  $[001]$  direction, with  $\varepsilon[001]=+1.1\%$ . From all these structural considerations, it is clear that the LCMO (110) films on STO (110) substrates are, in-plane, anisotropically strained. Similar results have been found for films of other thicknesses. We have reported elsewhere that this anisotropic strain gradually disappears as the film thickness increases.<sup>18</sup>

From the extracted values of  $d_{\text{LCMO}}[110]$ ,  $d_{\text{LCMO}}[1-10]$ , and  $d_{\text{LCMO}}[001]$  it follows that the unit cell is orthorhombic. The volume of the corresponding pseudocubic unit is  $58.1 \pm 0.1 \text{ \AA}^3$ . Since the volume of the pseudocubic unit cell of  $\text{La}_{2/3}\text{Ca}_{1/3}\text{MnO}_3$  is  $57.65 \text{ \AA}^3$ ,<sup>22</sup> the unit cell in our films appears to be slightly expanded with respect to bulk. We stress that this experimental observation contrasts with the common assumption that the Poisson law holds when evaluating cell parameters of manganite thin films.<sup>4,23</sup> The small expansion of the unit cell may reflect the existence of some oxygen deficiency.

In Fig. 3, a cross-section TEM image of the interface between a thin LCMO film (12 nm) and the STO (110) substrate is viewed along the  $[001]$  zone axis. The sharp contrast across the interface suggests the absence of interdiffusion. Fast Fourier transform images (FFT) (bottom panels) show  $[1-10]$  LCMO(110)// $[1-10]$  STO(110) epitaxial relationship and similar peaks for both the substrate and the manganite film, indicating the good epitaxy of manganite film.

After growing the LCMO (110) electrode on STO (110), STO upper layers of various thicknesses were subsequently grown. High-resolution TEM images of a STO/LCMO/STO bilayer have also been acquired. The cross-section TEM images along the  $[1-10]$  zone axis shown in Fig. 4 correspond to a bilayer formed by a LCMO bottom layer ( $t=21.5 \text{ nm}$ ) covered by STO top layer ( $t=27 \text{ nm}$ ). The STO layer/LCMO layer interface is in Fig. 4(a) and the LCMO layer/STO substrate one is in Fig. 4(b). No columnar defects in both LCMO and STO layers are observed and the corresponding interfaces are well defined. Fast Fourier transforms from LCMO and STO layers and STO(110) substrate (right panels) confirm the cube-on-cube epitaxial relationships in the two layers.

Magnetic and electronic homogeneity of an electrode in a MTJ is crucial for operation. Early experiments on LCMO

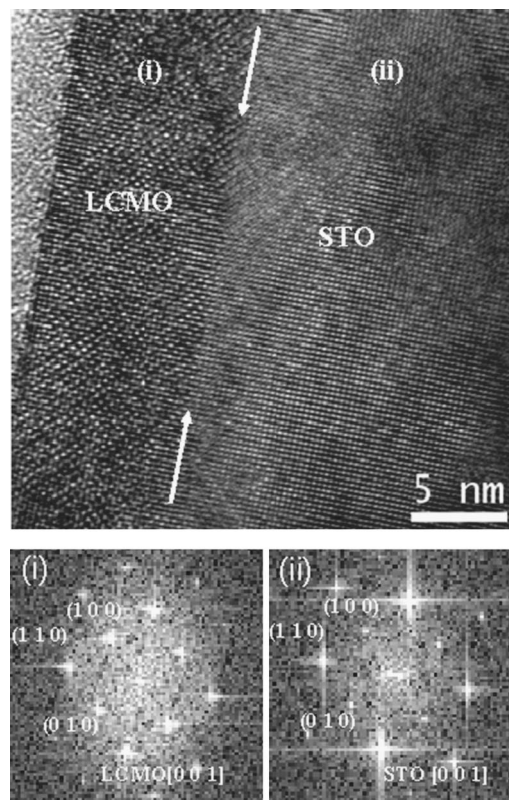


FIG. 3. Cross-section TEM image extracted from a 12 nm LCMO film along the  $[001]$  zone axis shows the absence of major defects in the manganite film and in the interface with the substrate (marked by arrows). Bottom panels: FFTs calculated from both the LCMO layer (i) and the STO substrate (ii).

(110) films, by using  $\text{Mn}^{55}$  NMR experiments,<sup>17</sup> indicated the absence of anomalous  $\text{Mn}^{m+}$  ( $\text{Mn}^{2+}$ ,  $\text{Mn}^{4+}$ ) states; only a signal corresponding to the mixed valence state  $\text{Mn}^{3+/4+}$  was detected. This observation, which contrasts with results reported for LCMO (001) films, where clear signatures of electronic inhomogeneities were detected,<sup>6,7</sup> provides an additional indication of the superior quality of LCMO (110) films. However, NMR gives volume-averaged signal, and unless very thin samples are used this technique is not particularly sensitive to the free surface. For that purpose, surface-sensitive techniques are more suitable to explore the eventual occurrence of chemical or electronic segregation. Thus, in order to get some information on the  $\text{Mn}^{m+}$  states at the film surface, XAS spectra of 11 nm thick (110) and (001) LCMO films were acquired. The experimental XAS results are compared with calculated spectra.

Figure 5 (top and center panels) shows the Mn 2p XAS spectra of LCMO films grown on STO (110) and (001). The spectra correspond to transitions from the Mn 2p level to unoccupied Mn 3d states. The spectra are split by spin-orbit interactions into the  $2p_{3/2}$  and  $2p_{1/2}$  regions. The Mn 2p XAS spectra are dominated by atomic multiplet and crystal field effects. The shape of the multiplet is directly related to the Mn 3d occupancy and the ground-state symmetry. The spectra can be calculated by the projection of the atomic multiplet in octahedral symmetry, as we described elsewhere.<sup>24</sup> The Mn 2p XAS spectra of  $\text{La}_{2/3}\text{Ca}_{1/3}\text{MnO}_3$  can be calculated by appropriate combination ( $2/3:1/3$ ) of the

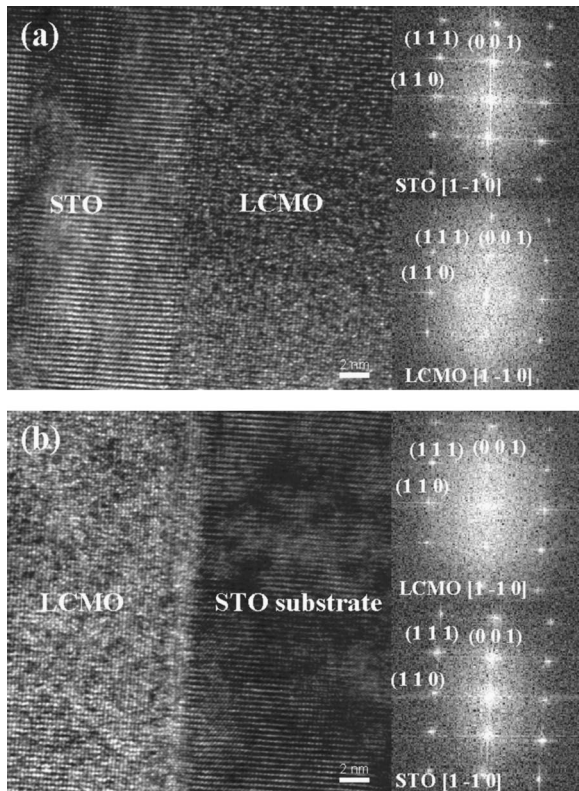


FIG. 4. Cross-section TEM images from a STO/LCMO/STO (110) bilayer along the  $[1-10]$  zone axis: (a) STO/LCMO interface, and FFTs calculated from each layer; (b) LCMO/substrate interface and FFTs calculated from the film and the substrate.

$2p^6 3d^n \rightarrow 2p^5 3d^{n+1}$  transitions in  $\text{LaMnO}_3$  and  $\text{CaMnO}_3$ . The ground state of the  $\text{Mn}^{3+}$  ion was  $t_{2g}^3 e_g^1 (^5E)$  with a crystal field of  $10Dq=2.4$  eV. The ground state of the  $\text{Mn}^{4+}$  ion was  $t_{2g}^3 (^4A_2)$  with a crystal field of  $10Dq=2.1$  eV. In Fig. 5 (bottom panel) we show the calculated spectrum. The agreement with the experimental ones is reasonably good, taking into account the neglect of lower symmetry effects. This shows that the Mn  $3d$ -O  $2p$  bonding is not affected by the substrate orientation. In turn, this suggests that the  $\text{MnO}_6$  octahedra are preserved as building blocks in the films. We stress that the experimental XAS spectra of these films are similar to those of the related  $\text{La}_{0.6}\text{Sr}_{0.4}\text{MnO}_3$  compound.<sup>24</sup> The presence of  $\text{Mn}^{2+}$  can be ruled out because, when present, the shape of the multiplet is completely different.<sup>24</sup>

Figure 6 shows the O  $1s$  XAS spectra of LCMO grown on STO (110) and (001). The spectra correspond to transitions from the O  $1s$  level to unoccupied O  $2p$  states. The spectra reflect, through hybridization, the different metal states in the conduction band. In particular, the structure at threshold corresponds to O  $2p$  character mixed with Mn  $3d$  states. The structure around 530–535 eV corresponds to the Mn  $3d$  band region; the features about 540 eV are related to the Ca  $3d$ /La  $5d$  states, whereas the higher energy bumps can be attributed to the empty Mn  $4sp$  bands. The overall shape of the spectra is similar to the O  $1s$  XAS spectrum of the similar  $\text{La}_{0.6}\text{Sr}_{0.4}\text{MnO}_3$  compound.<sup>24</sup> As in the case of Mn  $2p$  absorption, the XAS spectra can be calculated (not shown) using the O  $2p$  partial density of unoccupied states<sup>25</sup> and the mixing of  $2/3$   $\text{LaMnO}_3$  and  $1/3$   $\text{CaMnO}_4$  contribu-

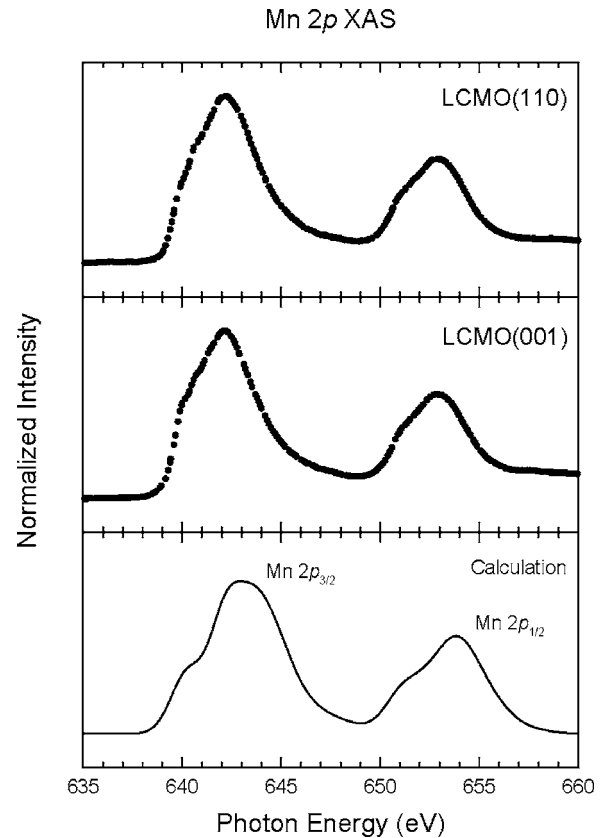


FIG. 5. Mn  $2p$  x-ray absorption spectra of LCMO films grown on (110) (top panel) and (001) STO (middle panel) compared to an atomic multiplet calculation (bottom panel).

tions. On the other hand, the O  $1s$  XAS spectra show differences in the C  $3d$ -La  $5d$  region; see Fig. 6. This is probably related to the different Ca-La termination in the (100) and (110) films, although differences in the Ca-La bonding at the LCMO/STO interface cannot be ruled out either.

The magnetic properties of LCMO (110) and (001) films were measured as a function of the temperature. The tem-

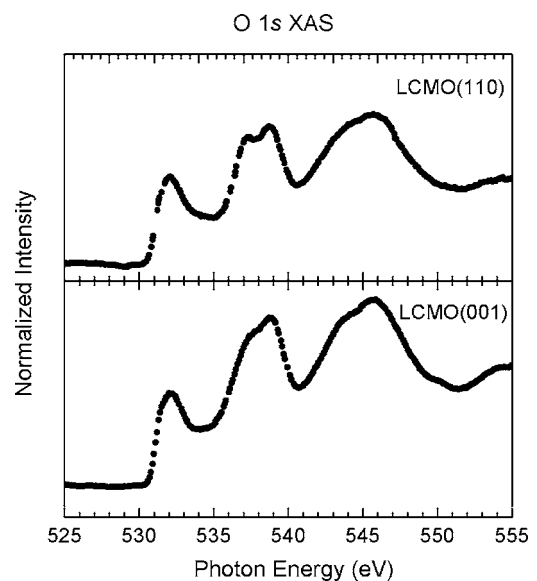


FIG. 6. O  $1s$  x-ray absorption spectra of LCMO films grown on (110) and (001) STO.



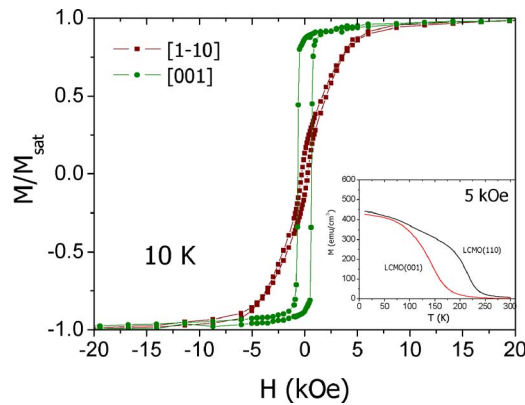


FIG. 7. Hysteresis loops obtained at 10 K of a  $t=17$  nm LCMO (110) film; magnetic field is applied in-plane. Easy axis is found to be along the [001] direction and hard axis along [1-10] Inset: temperature dependence of 17 nm (001) and (110) LCMO films measured at an applied in-plane field of 5 kOe.

perature dependence of magnetization of the LCMO (110) film is shown in Fig. 7 (inset).  $T_C$  is about 250 K, which, considering the small thickness of our film ( $\sim 17$  nm), is remarkably close to the bulk value ( $\sim 270$  K). This observation is dramatically emphasized when properties of LCMO (110) films are compared to those of a (001) film grown simultaneously, the magnetization curve of which is also shown in the inset of Fig. 7. The depression of magnetic properties, namely saturation magnetization and  $T_C$  in (001) films (in LCMO and similar manganites) when reducing thickness, is well documented.<sup>6,7,12</sup> Clearly, such reduction is absent in LCMO (110) films. Detailed discussion of this difference will be addressed elsewhere.<sup>18</sup>

We will focus now on the magnetic anisotropy of the films. The magnetic hysteresis loops of LCMO (110) films were measured with the magnetic field applied in the [1-10] and [001] in-plane directions (main panel in Fig. 7). There is a high in-plane uniaxial magnetic anisotropy in the (110) plane, in agreement with previously reported results on LCMO (Refs. 14–17) and other similar manganite films or heterostructures grown on STO (110).<sup>26,27</sup> XRD experiments allowed us to determine that the harder magnetic axis is parallel to the [1-10] direction, whereas the easy axis is along the [001] direction. Magnetotransport properties of LCMO (110) films, namely anisotropic magnetoresistance, have also provided evidence of in-plane uniaxial anisotropy.<sup>15,16</sup> Hysteresis loops measured along orthogonal directions in (110) films of increasing thickness display a progressive reduction of differences in magnetic anisotropy, suggesting that in-plane magnetic anisotropy is mainly determined by the uncommon anisotropic strain occurring in the (110) plane, as discussed elsewhere.<sup>18</sup> Prevalence of magnetoelastic over magnetocrystalline magnetic anisotropy in (110)  $\text{La}_{2/3}\text{Sr}_{1/3}\text{MnO}_3$  manganite films, was also reported by Berndt *et al.*;<sup>27</sup> the reverse was found in (001) films.

We turn next to the functional characterization of the STO (110) layer. Electric transport across an insulating thin layer can be explored by means of CAFM.<sup>28</sup> We have characterized by CAFM a bare  $t=19$  nm LCMO (110) electrode and STO/LCMO (110) bilayers with different barrier thick-

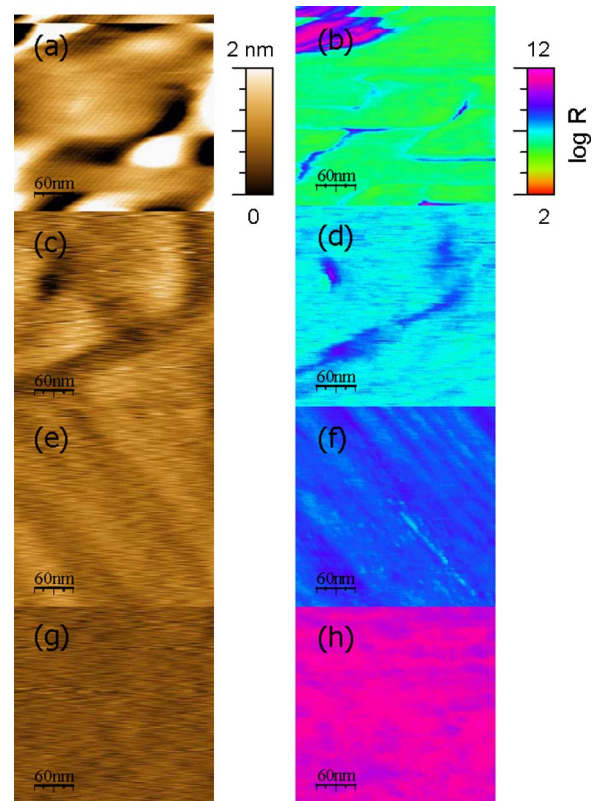


FIG. 8. Topographic images (left) and resistance maps (right) from a 19 nm LCMO electrode (a) and (b), and from bilayers presenting different STO thickness: (c) and (d) 0.85 nm, (e) and (f) 1.70 nm, and (g) and (h) 3.40 nm. Resistance maps were obtained at 2 V of polarization and they are plotted in logarithmic scale.

ness ( $t_{\text{STO}}=0.85, 1.70$ , and  $3.40$  nm). The corresponding topographic and resistance maps, simultaneously recorded under an applied bias ( $V$ ) of 2 V, are displayed in Fig. 8. CAFM requires the use of a coated tip, and it lowers the topographic image resolution; in spite of this, the most relevant morphological features of the film surface can still be observed. These features in topography are also observed in the resistance maps, due to local variations of the tip force or contact area. However, these changes in resistance are much smaller than the average variation between STO barriers of different thicknesses. Indeed, there is a huge increase of the measured resistance with the thickness of the barrier. It has to be noted that resistance maps are displayed in logarithmic scale, and that the local resistance of the order of  $10^6 \Omega$  in the bare electrode [Fig. 9(a)] increases up to around  $10^{11} \Omega$  for the  $t=3.4$  nm barrier [Fig. 8(c)]. From each resistance map, the corresponding resistance histograms are shown in Fig. 9(a). We note that for the STO layers, even with an increase in thickness of only 0.8 nm (nominally 2 u.c.) from one to the next, their corresponding histograms are well separated and with a moderate overlapping. This suggests that the insulating STO layer is covering homogeneously the LCMO electrode in the range of STO thickness studied.

Resistance maps allow us not only to evaluate the quality and homogeneity of STO barriers, but also to gain insight into the transport mechanism through them. From each histogram, the most probable resistance [maxima of the resistance histograms ( $R_m$ )] is used as a characteristic value of the

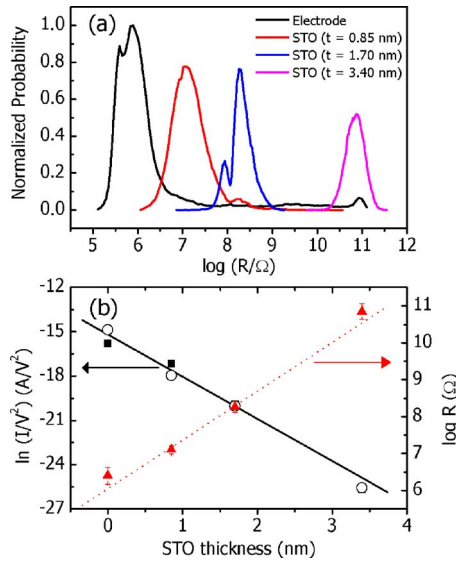


FIG. 9. (Color online) (a) Histograms presenting the different distribution of resistance values for a 19 nm LCMO (110) electrode and STO/LCMO (110) ( $t_{\text{STO}}=0.85, 1.70$ , and  $3.40$  nm) obtained under a 2 V polarization. (b) Right axis: Dependence of the maxima of the resistance in histograms of (a) vs STO barrier thickness (red triangles) and linear fit to these data (dashed red line). Left axis:  $(I/V^2)$  dependence on barrier thickness for the series of (110) films measured at 2 V (closed symbols) and corresponding linear fit (black solid line); results on LCMO (001) films and STO/LCMO (001) bilayers at the same polarization are also plotted (open symbols).

resistance through the corresponding barrier. In Fig. 9(b) (right axis) we depict directly the corresponding  $R_m$  values versus film thickness. The exponential increase of resistance with STO thickness signals that the conduction mechanism through the barrier corresponds to a tunneling process.

It is well known that current transport across tunnel barriers depends on the ratio  $V/\phi$ , where  $V$  is the bias voltage and  $\phi$  the effective energy barrier in the insulator.<sup>29</sup> Therefore, measurements under different bias voltages are commonly used to determine the tunnel regime and eventually the barrier height. Tunneling theory shows that if the potential barrier is far from being squarelike (Simmons limit) and for  $V > \phi$ , then the conduction occurs through a triangular-like barrier, and the tunneling conduction follows the so-called Fowler-Nordheim (FN) regime. The process then becomes exponentially dependent on voltage. The tunneling process is described through the FN expression,

$$I = \frac{2Ae^3}{8\pi h \beta^2 t^2 \phi_1} V^2 \exp\left(-\frac{8\pi\beta\sqrt{2m^*}\phi_1^{3/2}}{3he} \frac{1}{V} t\right), \quad (1)$$

where  $A$  is the effective contact area (tip-surface),  $m^*$  is the carrier effective mass (tunneling electron),  $\beta$  is a parameter which contains information about the shape of the potential barrier ( $\beta \sim 1$  for a rectangular barrier), and  $t$  is the barrier thickness. FN expression Eq. (2) can then be rewritten as

$$\ln \frac{I}{V^2} = \ln \left[ \frac{2Ae^3}{8\pi h \beta^2 t^2 \phi_1} \right] + Bt, \quad (2)$$

with

$$B = \frac{-8\pi\beta\sqrt{2m^*}\phi_1^{3/2}}{3he} \frac{1}{V}. \quad (3)$$

Equation (2) signals an exponential dependence of  $(I/V^2)$  on barrier thickness. In Fig. 9(b) (left axis) the calculated values of  $\ln(I/V^2)$  as a function of STO thickness (extracted from the associated experimental values of  $R_m$ , right axis) are plotted. The linear dependence of  $\ln(I/V^2)$  on thickness is quite visible. Moreover, Eq. (3) indicates that the slope ( $B$ ) of  $\ln(I/V^2)$  vs thickness ( $t$ ) should decrease as the bias increases. Therefore, the extraction of the effective energy barrier for tunneling ( $\phi$ ), or more precisely the term ( $m^*\phi$ ), requires the collection of data at several bias voltages. This information at the present stage is not yet available. However, the dependence of  $\ln(I/V^2)$  as a function of STO thickness for (110) STO barriers on LCMO (110) electrodes can be compared with the corresponding data collected on STO (001) barriers on LCMO (100) electrodes.<sup>28</sup> In Fig. 9(b) (left) we include the data extracted for CAFM resistance maps of STO (100) barriers which were grown simultaneously (open symbols). We note that the conductance of (001) and (110) STO barriers is very similar, thus suggesting a comparable energy barrier. Recently, we found that the energy barrier between the AFM tip and a STO barrier on a LCMO (001) is  $0.2\text{--}0.4$  eV,<sup>28</sup> and thus a similar height is expected in the case of the STO (110) barriers. This observation would imply that the band gaps in STO along [001] and [110] are similar. However, we note that calculations of the electronic band structure in STO showed that the theoretical energy gaps along these directions are 1.82 and 1.49 eV, respectively.<sup>30</sup>

#### IV. CONCLUSIONS

We have shown that LCMO (110) electrodes grown on STO (110) display magnetic properties which are improved with respect to simultaneously grown LCMO (001) counterparts: they present a higher Curie temperature and a weaker decay of magnetization when approaching  $T_C$ , and display in-plane uniaxial magnetic anisotropy. CAFM experiments have shown that STO layers on LCMO (110) electrodes, as thin as 0.8 nm, can be grown on top of it, displaying good insulating properties. The observation of tunnel transport through (110) STO barriers, and the very similar conductance to the (001) barriers, demonstrates that MTJs can be fabricated with (110)-oriented electrodes and barriers. The uniaxial magnetic anisotropy of the LCMO (110) electrodes offers clear advantage for device performance, and their robustness against electronic phase separation raises further hopes for manganite-based MTJs maintaining a large output at temperatures approaching the Curie transition.

#### ACKNOWLEDGMENTS

Financial support by the MEC of the Spanish Government (Projects NAN2004-9094-C03 and MAT2005-5656-C04), and by the EU [Project MaCoMuFi (No. FP6-33221) and FEDER] is acknowledged. The authors thank Dr. Manuel Bibes for helpful discussions.

<sup>1</sup>Y. Lu, X. W. Li, G. Q. Gong, G. Xiao, A. Gupta, P. Lecoeur, J. Z. Sun, Y. Wang, and V. P. Dravid, Phys. Rev. B **54**, R8357 (1996).

<sup>2</sup>M. Viret, M. Drouet, J. Nassar, J. P. Contour, C. Fermon, and A. Fert, Europhys. Lett. **39**, 545 (1997).

- <sup>3</sup>V. Garcia, M. Bibes, A. Barthélémy, M. Bowen, E. Jacquet, J.-P. Contour, and A. Fert, *Phys. Rev. B* **69**, 052403 (2004).
- <sup>4</sup>Y. Lu, J. Klein, F. Herbstritt, J. B. Philipp, A. Marx, and R. Gross, *Phys. Rev. B* **73**, 184406 (2006).
- <sup>5</sup>A. Moreo, S. Yunoki, and E. Dagotto, *Science* **283**, 2034 (1999).
- <sup>6</sup>M. Bibes, Ll. Balcells, S. Valencia, J. Fontcuberta, M. Wojcik, E. Jedryka, and S. Nadolski, *Phys. Rev. Lett.* **87**, 067210 (2001).
- <sup>7</sup>M. Bibes, S. Valencia, Ll. Balcells, B. Martínez, J. Fontcuberta, M. Wojcik, S. Nadolski, and E. Jedryka, *Phys. Rev. B* **66**, 134416 (2002).
- <sup>8</sup>J. Simon, T. Walther, W. Mader, J. Klein, D. Reisinger, L. Alff, and R. Gross, *Appl. Phys. Lett.* **84**, 3882 (2004).
- <sup>9</sup>T. Walther, *Ultramicroscopy* **96**, 401 (2003).
- <sup>10</sup>A. Ohtomo and H. Y. Hwang, *Nature* **427**, 423 (2004).
- <sup>11</sup>G. Koster, G. Rijnders, D. H. A. Blank, and H. Rogalla, *Physica C* **339**, 215 (2000).
- <sup>12</sup>J. L. Maurice, F. Pailloux, A. Barthélémy, A. Rocher, O. Durand, R. Lyonnet, and J. L. Contour, *Appl. Surf. Sci.* **188**, 176 (2002).
- <sup>13</sup>K. Steenbeck, T. Habisreuther, C. Dubourdieu, and J. P. Sénateur, *Appl. Phys. Lett.* **80**, 3361 (2002).
- <sup>14</sup>V. S. Amaral, A. A. C. S. Lourenço, J. P. Araújo, A. M. Pereira, J. B. Sousa, P. B. Tavares, J. M. Vieira, E. Alves, M. F. da Silva, and J. C. Soares, *J. Appl. Phys.* **87**, 5570 (2000).
- <sup>15</sup>I. C. Infante, V. Laukhin, F. Sánchez, and J. Fontcuberta, *Mater. Sci. Eng., B* **126**, 283 (2006).
- <sup>16</sup>I. C. Infante, D. Hrabovský, V. Laukhin, F. Sánchez, and J. Fontcuberta, *J. Appl. Phys.* **99**, 08C503 (2006).
- <sup>17</sup>J. Fontcuberta, I. C. Infante, V. Laukhin, F. Sánchez, M. Wojcik, and E. Jedryka, *J. Appl. Phys.* **99**, 08A701 (2006).
- <sup>18</sup>I. C. Infante *et al.* (unpublished).
- <sup>19</sup>Y. Y. Tse, R. I. Chakalov, M. M. Joshi, I. P. Jones, C. M. Muirhead, and R. Palai, *J. Phys.: Conf. Ser.* **26**, 115 (2006).
- <sup>20</sup>M. Abbate, J. B. Goedkoop, F. M. F. de Groot, M. Grioni, J. C. Fuggle, S. Hofmann, H. Petersen, and M. Sacchi, *Surf. Interface Anal.* **18**, 65 (1992).
- <sup>21</sup>Y. Mukunoki, N. Nakagawa, T. Susaki, and H. Y. Hwang, *Appl. Phys. Lett.* **86**, 171908 (2005).
- <sup>22</sup>Y. B. Zhang, S. Li, C. Q. Sun, and W. Gao, *Mater. Sci. Eng., B* **98**, 54 (2003).
- <sup>23</sup>Y. Lu, J. Klein, C. Höfener, B. Wiedenhorst, J. B. Philipp, F. Herbstritt, A. Marx, L. Alff, and R. Gross, *Phys. Rev. B* **62**, 15806 (2000).
- <sup>24</sup>M. Abbate, F. M. F. de Groot, J. C. Fuggle, A. Fujimori, Y. Tokura, Y. Fujishima, O. Strebel, M. Domke, G. Kaindl, J. van Elp, B. T. Thole, G. A. Sawatzky, M. Sacchi, and N. Tsuda, *Phys. Rev. B* **44**, 5419 (1991); M. Abbate, F. M. F. de Groot, J. C. Fuggle, A. Fujimori, O. Strebel, F. Lopez, M. Domke, G. Kaindl, G. A. Sawatzky, M. Takano, Y. Takeda, H. Eisaki, and S. Uchida, *ibid.* **46**, 4511 (1992).
- <sup>25</sup>F. M. F. de Groot, J. Faber, J. J. M. Michiels, M. T. Czyzyk, M. Abbate, and J. C. Fuggle, *Phys. Rev. B* **48**, 2074 (1993); M. Abbate, R. Potze, G. A. Sawatzky, and A. Fujimori, *ibid.* **49**, 7210 (1994).
- <sup>26</sup>Y. Suzuki, H. Y. Hwang, S.-W. Cheong, and R. B. van Dover, *Appl. Phys. Lett.* **71**, 140 (1997).
- <sup>27</sup>L. Berndt, V. Balbarin, and Y. Suzuki, *Appl. Phys. Lett.* **77**, 2903 (2000).
- <sup>28</sup>I. C. Infante, F. Sánchez, V. Laukhin, A. Pérez del Pino, J. Fontcuberta, K. Bouzehouane, S. Fusil, and A. Barthélémy, *Appl. Phys. Lett.* **89**, 172506 (2006).
- <sup>29</sup>J. G. Simmons, *J. Appl. Phys.* **34**, 2581 (1963); *J. Phys. D* **4**, 613 (1971).
- <sup>30</sup>T. Tanaka, K. Matsunaga, Y. Ikuhara, and T. Yamamoto, *Phys. Rev. B* **68**, 205213 (2003).